

Efficient micromirror confinement of sub-TeV cosmic rays in galaxy clusters

Patrick Reichherzer^{1,2*}, Archie F. A. Bott^{1,3}, Robert J. Ewart^{1,4},
 Gianluca Gregori^{1,5}, Philipp Kempski⁶, Matthew W. Kunz^{6,7}, and
 Alexander A. Schekochihin^{1,8}

¹Department of Physics, University of Oxford, Oxford OX1 3PU, UK.

²Exeter College, Oxford OX1 3DP, UK.

³Trinity College, Oxford OX1 3BH, UK.

⁴Balliol College, Oxford OX1 3BJ, UK.

⁵Lady Margaret Hall, Oxford OX2 6QA, UK.

⁶Department of Astrophysical Sciences, Princeton University, Peyton Hall, Princeton NJ 08544, USA.

⁷Princeton Plasma Physics Laboratory, Princeton University, PO Box 451, Princeton NJ 08543, USA.

⁸Merton College, Oxford OX1 4JD, UK.

*Corresponding author(s). E-mail(s): patrick.reichherzer@physics.ox.ac.uk;

Abstract

Recent observations suggest a stronger confinement of cosmic rays (CRs) in certain astrophysical systems than predicted by current CR-transport theories. We posit that the incorporation of microscale physics into CR-transport models can account for this enhanced CR confinement. We develop a theoretical description of the effect of magnetic microscale fluctuations originating from the mirror instability on macroscopic CR diffusion. We confirm our theory with large-dynamical-range simulations of CR transport in the intracluster medium (ICM) of galaxy clusters and kinetic simulations of CR transport in micromirror fields. We conclude that sub-TeV CR confinement in the ICM is far more effective than previously anticipated on the basis of Galactic-transport extrapolations.

Keywords: Cosmic Ray, Diffusion, Mirror Instability, Magnetic Mirror, Resonant Scattering, Galaxy Cluster

A good theory of cosmic-ray (CR) transport is crucial for advancing our understanding of phenomena in the Universe, including the formation and evolution of galaxies and galaxy clusters [42, 80]. CRs, through their transport characteristics, not only influence their environment but also modulate their own (re)acceleration efficiency [2, 10, 16, 17, 19, 96], confinement/escape [53, 81, 99],

spectra [33, 73], (an)isotropy [3], and observable photon [13, 18, 44] and neutrino [45] emission.

The transport characteristics of CRs in magnetic-field structures depend on the scattering efficiency and mechanism, both of which are influenced by the properties of the ambient plasma. Specifically, within a weakly collisional, high- β plasma, i.e., one in which the thermal

pressure much exceeds the magnetic pressure, deviations from local thermodynamic equilibrium provide free energy for fast-growing Larmor-scale instabilities, leading to distortions in magnetic fields on thermal-ion kinetic scales. In such a high- β plasma, two characteristic scales are relevant for describing the global transport of CRs: the macroscale correlation length l_c of the magnetic turbulence, and the microscale l_{mm} of the micromirrors¹ created by the mirror instability [65, 83]. While there are other micro-instabilities, the magnetic fluctuations created by the mirror instability are stronger and thus more influential for CR transport [15, 63]. The physics associated with these micro- and macroscales introduces three distinct transport regimes, which depend on the CR energy.

First, in the high-energy (he) limit, CRs with gyroradii $r_g \gg l_c$ (energies $E \gtrsim 100 \text{ EeV}$ for typical turbulence-driving scales in galaxy clusters) undergo scattering by small angles of the order $\delta\Theta \sim l_c/r_g$ at characteristic times $\delta t \sim l_c/c$, leading to a scattering rate $\nu_{\text{he}} \sim \delta\Theta^2/\delta t \sim cl_c/r_g^2$ and, therefore, to a CR diffusion coefficient $\kappa_{\text{he}} \sim c^2/\nu_{\text{he}} \sim cr_g^2/l_c \propto E^2/l_c$ [e.g., 4]. This scaling is indeed observed both in numerical simulations [e.g., 57, 76, 93] and (scaled) laboratory experiments [25] and serves as input for propagation models of ultra-high-energy CRs in galaxy clusters [29].

As the high-energy regime is, thus, believed to be understood, recent studies of CR transport have predominantly focused on the second, mesoscale regime, $r_g \lesssim l_c$, in which CRs scatter resonantly off inertial-range turbulent structures [36, 49, 54, 67]. This second regime is likely relevant for explaining CR spectra [6], e.g., the steepening of the CR spectrum in the Galactic Center from GeV to PeV energies [21, 32, 76, 100].

We argue, and confirm numerically, that in high- β plasmas, the presence of microstructures caused by plasma instabilities introduces a third regime, whose physics is similar to that of the first, but with the micromirror scale l_{mm} playing the role of l_c and the requirement that $r_g \gg l_{\text{mm}}$ ($E \gg 100 \text{ MeV}$). We show that this microscale physics

largely overrides the mesoscale resonant scattering and streaming. We apply our theory to the intracluster medium (ICM), a representative high- β plasma, and determine the transition between micro- and macrophysics-dominated transport to be at TeV energies, only weakly influenced by mesoscale physics. We confirm this theory with a novel method (described in Section 3) that incorporates the microscales ($l_{\text{mm}} \sim 100 \text{ npc}$), the macroscales ($l_c \sim 100 \text{ kpc}$), and the vast range in between.

1 Results

1.1 Effect of micromirrors on large-scale CR transport

It has long been realized that plasma instabilities may dominate the transport of low-energy CRs. However, the instabilities most often highlighted in the literature arise from the CRs themselves, rather than from the thermal plasma. One prominent example, especially for Galactic transport of CRs below 100 GeV, is the streaming instability [62]. This instability generates fluctuations in the magnetic field that in turn scatter the CRs and thereby reduce their streaming velocity to be comparable to the Alfvén speed in the plasma [11, 62, 85, 87]. By contrast, in high- β , weakly collisional plasmas, there exists a variety of instabilities that are driven by pressure anisotropies and generate magnetic fluctuations on ion-Larmor scales (see [65] and references therein). The pressure anisotropies arise from the (approximate) conservation of particle adiabatic invariants during the local stretching and compression of magnetic fields [26]. In the present context, the mirror instability [8, 41] is of particular interest because its saturated amplitude $\delta B_{\text{mm}} \sim B/3$ is of the same order of magnitude as the ambient magnetic field B [63, 68, 78].²

¹The prefix “micro” refers to scales much smaller than the $\gtrsim \mu\text{pc}$ gyroradii of $\gtrsim 100 \text{ MeV}$ CRs, and serves to distinguish the plasma-kinetic-scale “micromirrors” (l_{mm}) from the large-scale magnetic mirrors that also influence CR transport [22, 66, 75].

²By contrast, the other well-known instability arising in such plasmas, the firehose instability, is unlikely to affect CR transport because its expected saturation amplitude is small under ICM conditions: $\delta B_f \sim (\tau\Omega_i)^{-1/4} B$ [15, 63], where τ is the timescale over which a firehose-susceptible plasma evolves macroscopically, and $\Omega_i \sim 0.01 (B/3 \mu\text{G}) \text{ s}^{-1}$ is the non-relativistic thermal-ion gyrofrequency. In the ICM, $\tau\Omega_i \sim 10^{11}$ [79], so $\delta B_f \sim 10^{-3} B$. By analogy to (3), it follows that the CR scattering rate ν_f of CRs off firehoses in the ICM is much smaller than that off the mirrors: $\nu_f/\nu_{\text{mm}} \sim 10^{-7}$ (with the firehose scale taken to be comparable to the thermal-ion gyroradius [15, 63]).

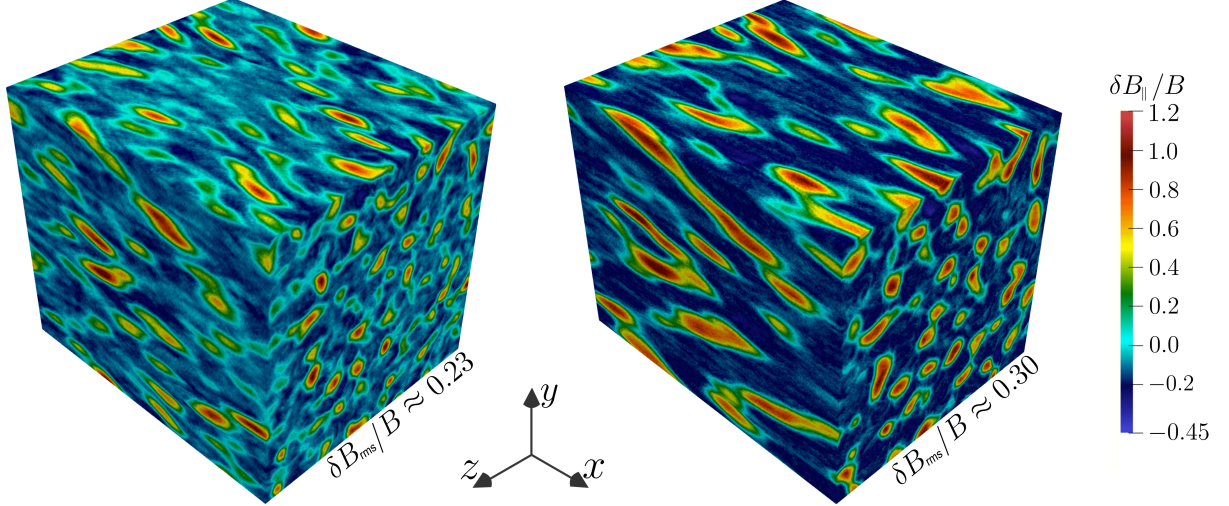


Fig. 1 The micromirror field generated by the PIC simulation discussed in the text: color shows fluctuations along (δB_{\parallel}) the field B , which is aligned with the x -axis. We show two snapshots of the 3D field during its secular evolution, characterized by the different $\delta B_{\text{rms}}/B$ (the right snapshot is later in the evolution).

To determine the impact of these micromirrors on CR transport, we begin by working out the relevant theoretical predictions for diffusion coefficients of CRs scattering at such strong fluctuations.³ The velocity change $\delta\mathbf{v}$ of a relativistic CR with gamma factor $\gamma = (1 - v^2/c^2)^{-1/2}$, charge $q = Ze$, and mass m in a magnetic-field structure of scale $l_{\text{mm}} \ll r_g$ and vector amplitude $\delta\mathbf{B}_{\text{mm}}$ is given in the small-angle limit $|\delta\mathbf{v}| \ll v$ by integrating the equation of motion $\gamma m d\mathbf{v}/dt = q(\mathbf{v}/c) \times \delta\mathbf{B}_{\text{mm}}$ along the CR path:

$$\delta\mathbf{v} \sim \frac{q}{\gamma mc v} \int_0^{l_{\text{mm}}} dl \mathbf{v} \times \delta\mathbf{B}_{\text{mm}}. \quad (1)$$

Assuming relativistic CRs with $v \approx c$, energy $E = \gamma mc^2$, and gyroradius $r_g = \gamma mc^2/qB$ determined by the ambient magnetic field $B \gtrsim \delta B_{\text{mm}}$, the scattering angle at characteristic times $\delta t \sim l_{\text{mm}}/c$ is

$$\delta\Theta \sim \frac{|\delta\mathbf{v}|}{c} \sim \frac{l_{\text{mm}}}{r_g} \frac{\delta B_{\text{mm}}}{B}. \quad (2)$$

Assuming that these small-angle deflections add up as a correlated random walk, the scattering

³A previous assumption of weaker micromirror fluctuations led to a different, much larger diffusion coefficient based on calculations using quasi-linear theory [40].

rate is

$$\nu_{\text{mm}} \sim \frac{\delta\Theta^2}{\delta t} \sim \frac{c l_{\text{mm}}}{r_g^2} \left(\frac{\delta B_{\text{mm}}}{B} \right)^2, \quad (3)$$

which implies a spatial diffusion coefficient of

$$\kappa_{\text{mm}} \sim \frac{c^2}{\nu_{\text{mm}}} \sim \frac{c r_g^2}{l_{\text{mm}}} \left(\frac{\delta B_{\text{mm}}}{B} \right)^{-2} \propto E^2 l_{\text{mm}}^{-1}. \quad (4)$$

As usual, more energetic CRs diffuse much faster.

In arriving at (4), we effectively assumed that micromirrors are described by only one characteristic scale, l_{mm} . In reality, micromirrors are anisotropic (see ellipsoid-like shapes in Figure 1) with scales perpendicular (\perp) and parallel (\parallel) to the ambient magnetic field that satisfy $l_{\perp,\text{mm}} \ll l_{\parallel,\text{mm}}$. While gyrating through this field, CRs with $r_g \gg l_{\text{mm}}$ mostly traverse micromirrors perpendicularly⁴. For $r_g \gg l_{\perp,\text{mm}}$, CRs will sample many different micromirrors, with deflections adding up as a correlated random walk⁵. The scattering rate

⁴Only low-energy CRs satisfying $r_g v_{\perp}/c \lesssim l_{\perp,\text{mm}} \ll l_{\parallel,\text{mm}}$ are an exception and should be treated analogously to thermal electrons with negligible r_g getting scattered [78, 101] and trapped [56] in the micromirrors. This subpopulation makes a negligible contribution to the overall transport of CRs with $r_g \gg l_{\perp,\text{mm}}$ considered here.

⁵During one gyro-orbit, CRs will travel $\Delta l_{\parallel} \sim 2\pi r_g v_{\parallel}/c$ in the field-parallel direction. CRs with large pitch angles satisfying $\Delta l_{\parallel} \lesssim l_{\parallel,\text{mm}}$, i.e., $v_{\perp}/v_{\parallel} \sim c/v_{\parallel} \gtrsim 2\pi r_g/l_{\parallel,\text{mm}}$, that sample the same micromirror repeatedly, may become relevant only at low energies $r_g \lesssim l_{\parallel,\text{mm}}/2\pi$, not considered in this study.

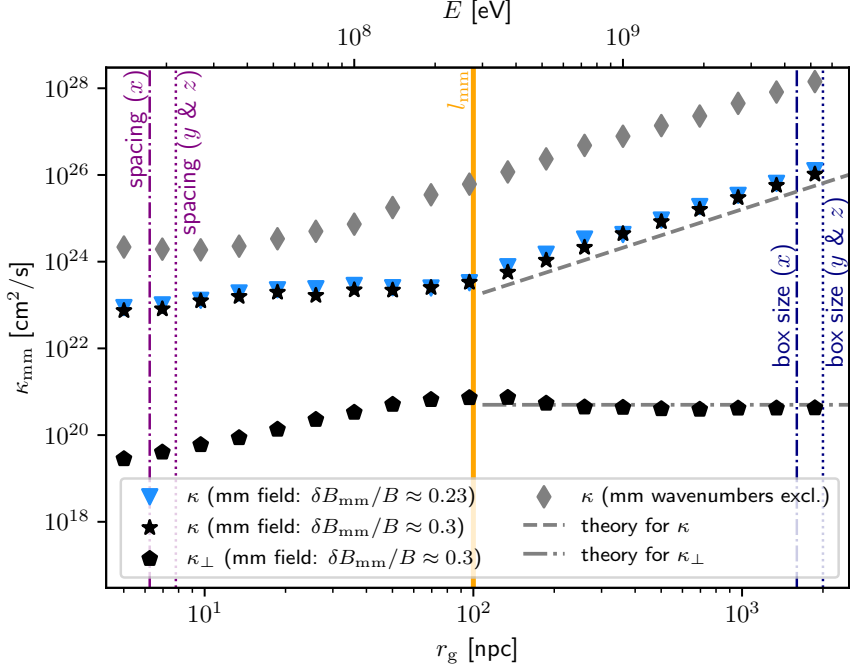


Fig. 2 Diffusion coefficients of CRs in the micromirror fields presented in Figure 1. The diffusion coefficient κ is dominated by the parallel diffusion, the perpendicular diffusion coefficient κ_{\perp} is negligible. Our predictions (5) (gray dashed line) and (6) (gray dash-dotted line), valid for $l_{\text{mm}} \ll r_g$, agree well with the computed diffusion coefficients. Note that κ decreases with $\delta B_{\text{mm}}/B$ (triangles vs. stars). We include results for CRs with gyroradii smaller than the micromirror scale l_{mm} to highlight the change in transport regimes, which follows from our theory. The gray markers show the transport of CRs through the residual field that results after filtering out the wavenumbers associated with the micromirrors, leaving only numerical noise. The purple vertical (dash-)dotted lines show grid resolution and box sizes along the three axes. $Z = 1$ is used for the energy scale.

associated with the parallel micromirror perturbation $\delta B_{\parallel} \sim B_{\text{mm}}$ decreases with decreasing pitch angle, but this is overcome by scattering at the perpendicular micromirror component $\delta B_{\perp} \sim \delta B_{\parallel} l_{\perp,\text{mm}}/l_{\parallel,\text{mm}}$ for $v_{\perp}/v_{\parallel} \lesssim l_{\perp,\text{mm}}/l_{\parallel,\text{mm}} \ll 1$. Except for this cone containing CRs with small pitch angles, from which they escape quickly on the time scale $t_{\text{esc}} \sim \nu_{\text{mm}}^{-1} l_{\perp,\text{mm}}/l_{\parallel,\text{mm}}$, gyrating CRs cross micromirrors perpendicularly faster than they traverse them in the parallel direction, implying $l_{\text{mm}} \sim l_{\perp,\text{mm}}$ to be the relevant scale.

For application to the ICM, we estimate l_{mm} using an asymptotic theory of the mirror instability's nonlinear evolution [77] supported by previous numerical studies [63, 70]: $l_{\text{mm}} \sim (\tau \Omega_i)^{1/8} r_{g,i}$, where τ is the timescale over which a micromirror-susceptible plasma evolves macroscopically. Applying the theory to an ICM [39, 65] with $B \sim 3 \mu\text{G}$, the thermal-ion gyroradius $r_{g,i} \sim (2T/m_i)^{1/2}/\Omega_i \sim 1 \text{ npc}$, the mean galaxy cluster temperature $T \sim 5 \text{ keV}$, the thermal-ion mass m_i ,

and $\tau \sim 10^{12} \text{ s}$ [77, 79] yields $l_{\text{mm}} \sim l_{\perp,\text{mm}} \sim 100 r_{g,i} \sim 100 \text{ npc}$ [70], only a factor of few smaller than the gyroradius of a GeV CR. In combination with (4), this gives us the estimate

$$\begin{aligned} \kappa_{\text{mm}} &\sim 10^{30} Z^{-2} \left(\frac{l_{\text{mm}}}{100 \text{ npc}} \right)^{-1} \left(\frac{B}{3 \mu\text{G}} \right)^{-2} \\ &\quad \times \left(\frac{\delta B_{\text{mm}}/B}{1/3} \right)^{-2} \left(\frac{E}{\text{TeV}} \right)^2 \text{ cm}^2 \text{ s}^{-1}, \\ &\sim 10^{30} Z^{-2} \left(\frac{T}{5 \text{ keV}} \right)^{-1/2} \left(\frac{B}{3 \mu\text{G}} \right)^{-1} \\ &\quad \times \left(\frac{\delta B_{\text{mm}}/B}{1/3} \right)^{-2} \left(\frac{E}{\text{TeV}} \right)^2 \text{ cm}^2 \text{ s}^{-1}. \end{aligned} \quad (5)$$

This estimate is valid provided $l_{\text{mm}} \ll r_g$ and $\delta t \nu_{\text{mm}} \sim (l_{\text{mm}}/r_g)^2 (\delta B_{\text{mm}}/B)^2 \ll 1$ ($E \gg 100 \text{ MeV}$).

We now show that the diffusion coefficient (5) is associated with parallel transport along field lines by demonstrating that the perpendicular diffusion coefficient is negligible. Each scattering at characteristic times $\delta t \sim l_{\text{mm}}/c$ moves the gyrocenter by a distance $\Delta r_{\perp} \sim r_g \delta \Theta$ in the plane perpendicular to the local magnetic field line. Using the estimate (2) for the scattering angle leads to the perpendicular diffusion coefficient

$$\begin{aligned}\kappa_{\perp,\text{mm}} &\sim \frac{\Delta r_{\perp}^2}{\delta t} \sim \frac{r_g^2 \delta \Theta^2}{l_{\text{mm}}/c} \sim c l_{\text{mm}} \left(\frac{\delta B_{\text{mm}}}{B} \right)^2 \\ &\sim \frac{l_{\text{mm}}^2}{r_g^2} \left(\frac{\delta B_{\text{mm}}}{B} \right)^4 \kappa_{\text{mm}}.\end{aligned}\quad (6)$$

Since $\kappa_{\perp,\text{mm}} \ll \kappa_{\text{mm}}$ for $r_g \gg l_{\text{mm}}$ and $\delta B_{\text{mm}} \lesssim B$, it is the parallel diffusion $\kappa_{\parallel,\text{mm}} \sim \kappa_{\text{mm}}$ along field lines that dominates.

To validate our theoretical prediction for the diffusion coefficients (5) and (6), we performed a numerical experiment in which a spectrum of CRs was integrated in a magnetic field containing micromirrors generated self-consistently via a particle-in-cell (PIC) simulation (Section 3.6). For our numerical experiment, we selected two representative realizations of the 3D field during its secular evolution, visualized in Figure 1. We then determined the diffusion coefficients of the CRs in both fields by integrating the CR equation of motion. The results are shown in Figure 2. The diffusion coefficients in the micromirror fields show good agreement with (5) and (6).

1.2 The micro-macrophysics transition is at TeV CR energies

In Section 1.1, we derived the diffusion coefficient $\kappa_{\text{mm}} \propto l_{\text{mm}}^{-1} E^2$ associated with CR scattering at micromirrors of scale l_{mm} . To determine the upper bound for the energies at which the scattering off micromirrors dominates CR transport, one needs a model of the competing contribution to it from the resonant scattering off mesoscale magnetic turbulence. In Section 3.4, we present models of CR diffusion based on resonant scattering in the (mesoscale) inertial range of magnetic turbulence stirred at the macroscale l_c , leading to the diffusion coefficient

$$\kappa_{\text{res}} \sim c l_c \left(\frac{r_g}{l_c} \right)^{\delta} \propto E^{\delta} l_c^{-\delta+1}, \quad (7)$$

where the model-dependent exponent is $0 \leq \delta \leq 1/2$ (Section 3.4). The mechanism with the smallest diffusion coefficient dominates CR transport. The transition between the micromirror and resonant-scattering transport regimes occurs when $\kappa_{\text{mm}} \sim \kappa_{\text{res}}$. Equating (4) and (7) determines the gyroradius corresponding to this transition:

$$r_g \sim l_c \left(\frac{\delta B_{\text{mm}}}{B} \right)^{2/(2-\delta)} \left(\frac{l_{\text{mm}}}{l_c} \right)^{1/(2-\delta)}. \quad (8)$$

This translates into a δ -dependent estimate for the transition energy:

$$E \sim Z \left(\frac{B}{3 \mu\text{G}} \right) \left(\frac{l_c}{100 \text{kpc}} \right) \times \begin{cases} 300 \left(\frac{\delta B_{\text{mm}}}{B} \right)^{2/(2-\delta)} \left(\frac{l_{\text{mm}}}{l_c} \right)^{1/(2-\delta)} \text{EeV}, & \text{general } \delta, \\ 5 \left(\frac{\delta B_{\text{mm}}/B}{1/3} \right)^{6/5} \left(\frac{l_{\text{mm}}/l_c}{10^{-12}} \right)^{3/5} \text{TeV}, & \delta = 1/3, \\ 600 \left(\frac{\delta B_{\text{mm}}/B}{1/3} \right)^{4/3} \left(\frac{l_{\text{mm}}/l_c}{10^{-12}} \right)^{2/3} \text{GeV}, & \delta = 1/2. \end{cases} \quad (9)$$

Below this energy, magnetic micromirrors dominate CR diffusion. The factor involving the ratio l_{mm}/l_c accounts for the scale separation between micro- and macrophysics, which we estimate to be $\sim 10^{-12}$ in the ICM.

To test this prediction, we performed numerical simulations of CR transport in the ICM (detailed in Section 3), modeling the effects of both the micromirrors (Section 3.3) and of the turbulent cascade up to $l_c \sim 100$ kpc (Section 3.4). Figure 3 summarizes our results by presenting the

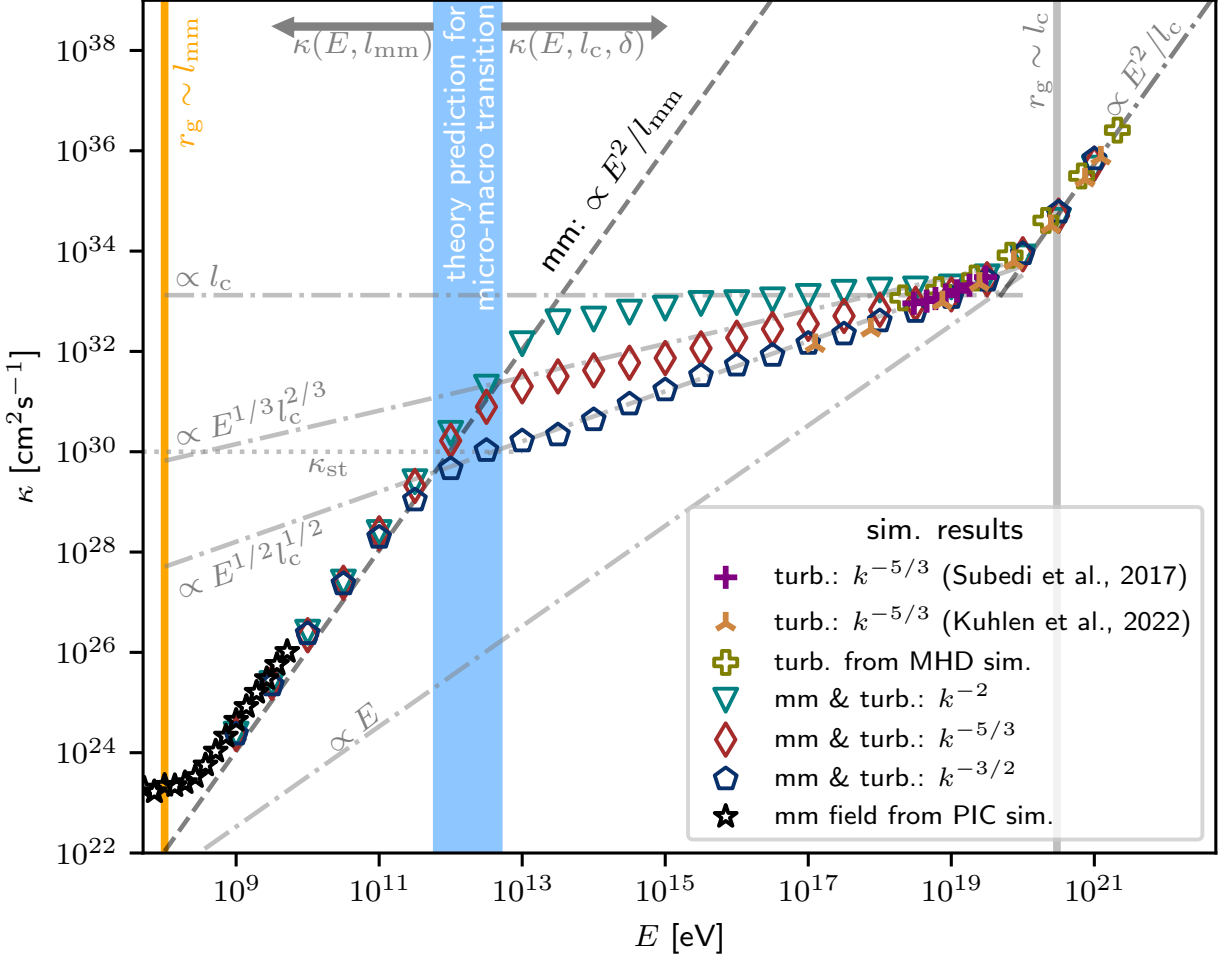


Fig. 3 CR diffusion coefficients (Section 3.5) of cosmic rays (CRs) with $Z = 1$ in the ICM displayed as functions of CR energy for a number of model turbulence spectra. These diffusion coefficients are calculated from simulated CR trajectories, taking into account their equation of motion and scattering by micromirrors (mm) (Section 3). The black stars show the diffusion coefficients in the micromirror field generated by a PIC simulation (Section 3.6). The olive empty crosses show the diffusion coefficients of CRs in MHD turbulence without a guide field (Section 3.7). The other empty markers show the diffusion coefficients computed in isotropic synthetic turbulence with a large inertial range (Section 3.1), together with our stochastic micromirror-scattering model (Section 3.3). The grey dash-dotted lines represent theories for CR transport depending on the macroscale l_c according to (7), including the most efficient (Bohm) and the least efficient (energy-independent) diffusion scenarios. The grey dotted line represents the diffusion due to streaming instability, according to (14). The grey dashed line represents our prediction of the diffusion due to micromirrors according to (5). The vertical light-blue bar indicates our estimate (9) for the micro-macro transition for the most likely range of δ values between $1/3$ and $1/2$. Simulation results from Subedi et al. [93] and Kuhlen et al. [61] illustrate the best resolution towards the limit $r_g \ll l_c$ achieved prior to the present results with synthetic turbulence on a grid (2048^3 grid points) and nested grids, respectively.

CR diffusion coefficient as a function of energy. The vertical light-blue bar indicates our estimate (9) for the micro-macro transition assuming the most likely range of $\delta \in [1/3, 1/2]$. While this estimate of the micro-macrophysics transition at TeV CR energies is numerically confirmed using synthetic turbulence, we also used magnetic fields

from direct PIC and MHD simulations to validate the consistency of our numerical approach at micro- and macroscales, respectively, and capture all relevant diffusion coefficients discussed in the literature, and detailed as points (i) to (iii) in Section 3.4.

1.3 Case of spatially intermittent micromirrors

Thus far, we have effectively assumed that the micromirrors permeate the plasma uniformly. In reality, the situation is more complicated: micromirrors will most likely appear in spatially intermittent and temporally transient patches wherever turbulence leads to local amplification of the magnetic field at a rate that is sufficiently large to engender positive pressure anisotropy exceeding the mirror-instability threshold ($\sim 1/\beta$; see, e.g., [70, 90] and references therein). This gives rise to an effectively two-phase plasma, with two different effective scattering rates: $\nu_{\text{mm}} \sim c^2/\kappa_{\text{mm}}$ in micromirror patches and $\nu_{\text{res}} \sim c^2/\kappa_{\text{res}}$ elsewhere (instead of κ_{res} , one could also use κ_{st} associated with the streaming instability – see Section 2). For the purpose of modeling CR scattering in such a plasma, we introduce the effective micromirror fraction f_{mm} to quantify the probability of CR being scattered by the micromirrors. By definition, the effective scattering rate in a two-phase medium is [51, 58]:

$$\nu_{\text{eff}} = f_{\text{mm}} \nu_{\text{mm}} + (1 - f_{\text{mm}}) \nu_{\text{res}}. \quad (10)$$

The effective diffusion coefficient is then

$$\kappa_{\text{eff}} \sim \frac{\kappa_{\text{mm}}}{f_{\text{mm}} + (1 - f_{\text{mm}})\kappa_{\text{mm}}/\kappa_{\text{res}}}. \quad (11)$$

The transition at which micromirror transport takes over from resonant scattering is entirely independent of f_{mm} : $\kappa_{\text{eff}} \sim \kappa_{\text{res}}$ when $\kappa_{\text{mm}} \sim \kappa_{\text{res}}$. However, the asymptotic scaling $\kappa_{\text{eff}} \sim \kappa_{\text{mm}}/f_{\text{mm}}$ is only reached at CR energies for which $\kappa_{\text{mm}}/\kappa_{\text{res}} \lesssim f_{\text{mm}}/(1 - f_{\text{mm}})$, pulling the transition energy down by a factor of $f_{\text{mm}}^{1/(2-\delta)}$. This is not a very strong modification of our cruder ($f_{\text{mm}} = 1$) estimate (9) unless f_{mm} is extremely small.

The most intuitive interpretation of f_{mm} is that it is the fraction of the plasma volume occupied by the micromirrors. This, however, requires at least two caveats: (i) the lifetime of micromirror patches, determined by the turbulent dynamics, can be shorter than the time for a CR to diffuse through the patch; (ii) if the micromirror patches form solid macroscopically extended three-dimensional blobs, it is possible to show

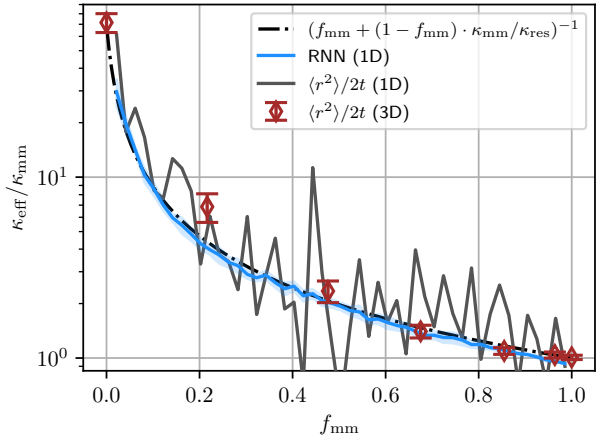


Fig. 4 Effective diffusion coefficient of charged particles in a two-phase medium vs. the effective micromirror fraction f_{mm} modeled by the volume-filling fraction of magnetic fields whose strength exceeds a certain threshold (see Section 3.8). We model the CR transport through a two-phase medium in 3D and 1D (to reduce simulation costs), as explained in Section 3.8. The 3D case (red diamonds) shows the diffusion coefficient of 300 GeV CRs computed at their trajectory lengths of $\simeq 10l_c$. The blue and black lines with corresponding error bands show the 1D results on 400 test trajectories using our recurrent neural network (RNN) and the classical analysis method. The dash-dotted black line represents expected values for averaged scattering frequencies of CRs in the two-phase plasma, formally expressed in (11). The diffusion coefficients κ_{mm} and κ_{res} are recovered for $f_{\text{mm}} = 1$ and $f_{\text{mm}} = 0$, respectively.

that CRs typically do not penetrate much farther than λ_{mm} into the patches. This leaves the patch volume largely uncharted (see Appendix 3 in [58]). The second concern obviates the first (see Section 3.8). Note that under such a scenario, the effective CR diffusion in the ICM might be determined primarily by such factors as the typical size of the patches and the distance between them [20]. However, the scenario of micromirror-dominated transport is made more plausible as the diffusion is mostly along the field line, which will guide CRs naturally into and out of the micromirror patches, especially if the two phases of the scattering medium intertwine narrowly. For example, with micromirror patches forming sheet-like structures – in a turbulent environment, where those patches should coincide with regions of greatest amplification of the magnetic field, such a scenario appears most likely.

Indeed, our model formula (11) proves to be a good prediction even in a simple modification of our numerical experiment with synthetic fields, designed to model micromirror patches (see Section 3.8). Its results are shown in Figure 4. It is a matter of future work to determine the precise dependence of f_{mm} on the morphology and dynamics of magnetic fields and micromirror-unstable patches in high- β turbulence – itself a system that has only recently become amenable to numerical modeling [7, 90]. Here, we proceed to discuss the implications of dominant micromirror transport, assuming that f_{mm} is not tiny.

2 Discussion

We have argued that CR diffusion in the ICM is determined by microscale (l_{mm}) mirrors at energies $E \lesssim \text{TeV}$ and by macroscale (l_c) turbulence at $E \gtrsim \text{TeV}$. Although the micro-macrophysics transition mainly depends on these two scales, there is a degree of fine-tuning at mesoscales. This refers to the role played in (9) by the exponent δ , which depends on the details of the scattering mechanism and of the turbulent cascade (see Section 3.4). While our study is tailored to the ICM, it can be adapted to other nearly collisionless high- β plasmas, such as the hot interstellar medium and the Milky Way halo.

Let us now discuss the self-confinement of CRs due to the streaming instability, believed to play an important role in the Galaxy [11] and in galaxy clusters [47]. In this picture, the streaming instability generates fluctuations of the magnetic field, which in turn can scatter CRs. It is believed that this mechanism may take over at lower CR energies, with details depending on the instability's growth rate at wavenumber k [62]:

$$\begin{aligned} \gamma_{\text{SI}} &\sim \Omega_i \frac{n_{\text{CR}}(>E)}{n_i} \left(\frac{v_{\text{st}}}{v_A} - 1 \right) \\ &\sim 10^{-14} \left(\frac{B}{3 \mu\text{G}} \right) \left(\frac{E}{\text{TeV}} \right)^{-1.6} \text{ s}^{-1}, \end{aligned} \quad (12)$$

where $n_{\text{CR}}(>E)$ is the density of CRs with energies above energy E corresponding to the resonance condition that can interact resonantly with waves with wavenumber k , n_i is the ambient ion density, v_A is the Alfvén speed, and v_{st} is the streaming speed, believed to be on the order of v_A

in saturation for the $\sim \text{GeV}$ CRs [47, 60]. In the second estimate in (12), we employed the common assumptions (see, e.g., [53, 102] and references therein) that $v_{\text{st}}/v_A \sim 1$ and $n_{\text{CR}}(>E)/n_i \sim 10^{-7}(E/\text{GeV})^{1-\alpha}$ in galaxy clusters, with $\alpha \approx 2.6$.

Scattering of sub-TeV CRs at micromirrors increases the effective CR collisionality in high- β environments. This could potentially undermine the CR streaming instability. A comparison of the growth rate (12) with the scattering rate at micromirrors (3) gives

$$\begin{aligned} \frac{\gamma_{\text{SI}}}{\nu_{\text{mm}}} &\sim 10^{-5} Z^{-2} \left(\frac{T}{5 \text{ keV}} \right)^{-1/2} \\ &\times \left(\frac{\delta B_{\text{mm}}/B}{1/3} \right)^{-2} \left(\frac{E}{\text{TeV}} \right)^{0.4}. \end{aligned} \quad (13)$$

With such a large effective collisionality isotropizing and homogenizing CRs, it is doubtful that a collisionless, resonant instability can operate.

Another way to gauge the importance of the streaming instability is to compare the putative CR diffusion coefficient κ_{st} due to it with κ_{mm} at the same energies. Let us pretend that the instability is not suppressed, despite (13), estimating κ_{st} in an environment with magnetic-field lines stochastically tangled on the scale l_c [60, 93]:

$$\begin{aligned} \kappa_{\text{st}} &\sim l_c v_{\text{st}} \gtrsim l_c v_A \\ &\sim 10^{30} \left(\frac{l_c}{100 \text{ kpc}} \right) \left(\frac{v_A}{100 \text{ km/s}} \right) \text{ cm}^2 \text{ s}^{-1}, \end{aligned} \quad (14)$$

where we have used the Alfvén speed $v_A \sim 100 \text{ km/s}$ as the lower limit of the streaming speed. Comparing this CR diffusivity with the one caused by micromirrors (5) gives

$$\begin{aligned} \frac{\kappa_{\text{mm}}}{\kappa_{\text{st}}} &\sim Z^{-2} \left(\frac{E}{\text{TeV}} \right)^2 \left(\frac{l_c}{100 \text{ kpc}} \right)^{-1} \left(\frac{v_A}{100 \text{ km/s}} \right)^{-1} \\ &\times \left(\frac{B}{3 \mu\text{G}} \right)^{-1} \left(\frac{\delta B_{\text{mm}}/B}{1/3} \right)^{-2} \left(\frac{T}{5 \text{ keV}} \right)^{-1/2}, \end{aligned} \quad (15)$$

demonstrating that κ_{mm} dominates CR transport in the ICM up to TeV energies. Note that the effective Alfvén speed is increased due to positive pressure anisotropy in micromirror patches [14, 64, 103], which should reduce the growth rate (12) of

the streaming instability and further increase the resulting CR diffusion coefficient (14). While the suppressed streaming instability within micromirror regions of the ICM challenges the universal applicability of the prevailing models that seek to explain the thermal balance between heating and cooling of galaxy clusters based on collisionless, resonant mechanisms [47, 48], a patchy distribution of these micromirrors may allow for the existence of regions where the streaming instability remains active – indeed possibly more so than usually expected, as those micromirror-free regions are likely to feature negative pressure anisotropies and, therefore, reduced effective Alfvén speeds.

With this revised picture of CR diffusion in the ICM, we can discuss the emission signatures of diffusing CRs within galaxy clusters. Galaxy clusters have been identified as potentially significant contributors to the observed diffuse gamma-ray background through hadronic interactions of CR protons with background gas and photons (see, e.g., references in [30]). However, direct observations of diffuse gamma-ray emission from galaxy clusters remain elusive [30]. Our model offers a viable explanation for this non-detection: micromirrors in the ICM confine sub-TeV CR protons near their emission sources within galaxy clusters. This should result in (extended) point-like gamma-ray emission rather than widespread diffuse emission, as indeed observed in [1, 74]. While this suggests a similar confinement of CR electrons, the prevalent synchrotron radiation in some galaxy clusters, evident in the form of large radio halos, could be attributed, e.g., to electron reacceleration processes⁶ [30] or to secondary electrons that might be produced by interactions between very-high-energy gamma rays and diffuse background radiation [95].

Finally, the suppressed CR diffusion coefficient due to micromirrors offers a compelling explanation for how CRs can be effectively “frozen” within the ICM as key parameters such as gas density

⁶The reduction in diffusion coefficients due to micromirror scattering does not necessarily promote the reacceleration of CRs. Because the phase velocity of the micromirrors is zero in the rest frame of the plasma, the motions of the effective scattering sites are tied to the bulk flow. Nevertheless, an effective non-resonant second-order Fermi acceleration may occur in compressible turbulence when the diffusion coefficient is comparable to the product of the sound speed and the scale of the compressing wave, so that CRs can random walk in energy with energy gains (losses) when confined during compressions (rarefactions) with a net energy gain [19].

and magnetic-field intensity evolve, an assumption fundamental to recent models of the dynamical evolution of galaxy clusters and their surroundings [10, 13, 31]. This impacts the interplay between CRs and the broader astrophysical mechanisms within these massive cosmic structures.

3 Methods

Modeling CR transport across a wide energy spectrum from GeV to EeV energies in a multi-scale high- β plasma presents methodological and computational challenges. For our numerical simulations, we choose parameters from the ICM, a high- β plasma. Rotation-measure data indicate magnetic-field strengths $\sim 0.1\text{--}1\,\mu\text{G}$ averaged over a Mpc^3 ICM volume [39, 92], with typical field strengths of several μG in central regions [e.g., 12]. Numerical simulations support these estimates [e.g., 91]. We choose $B \sim 3\,\mu\text{G}$, $\delta B_{\text{mm}}/B \sim 1/3$, the micromirror scale $l_{\text{mm}} \sim 100\,\text{npc}$, and turbulence correlation length $l_c \sim 100\,\text{kpc}$ [65]. Simulations are performed using the publicly available tool CRPropa 3.2 [5] with additional extensions and modeling choices described below.

3.1 Model of synthetic magnetic turbulence

Modeling the competing micro- and macrophysical transport effects requires resolving turbulence over at least ten decades in scale. Current MHD and PIC simulations are unsuitable for this as they only allow for limited scale ranges [71]. Even the current best grid resolutions of more than 10^{12} cells resolve less than four decades in scale separation. Synthetic turbulence, on the other hand, can be generated by summing over n_m plane waves at an arbitrary particle position \mathbf{r} as follows [36, 94]

$$\begin{aligned} \delta\mathbf{B}(\mathbf{r}) &= \text{Re} \left(\sum_{n=1}^{n_m} \delta\mathbf{B}_n^* e^{i\mathbf{k}_n \cdot \mathbf{r}} \right) \\ &= \sqrt{2} \delta B \sum_{n=1}^{n_m} \xi_n A_n \cos \left(k_n \hat{\mathbf{k}}_n \cdot \mathbf{r} + \phi_n \right), \end{aligned} \quad (16)$$

with normalized amplitudes A_n determined by the assumed turbulent energy spectrum, uniformly distributed phase factors $\phi_n \in [0, 2\pi]$, unit

wavevectors $\hat{\mathbf{k}}_n$, and polarizations ξ_n , satisfying $\hat{\mathbf{k}}_n \cdot \xi_n = 0$. We employ the performance-optimized method described in [84]. We investigated the number of wavemodes n_m needed by analyzing turbulence characteristics and diffusion coefficients of CRs and found that $n_m = 1024$ log-spaced wavemodes are sufficient.

We compared our key results on CR transport obtained with the above method with those obtained with an alternative method for synthetic turbulence, where we followed the approach proposed, e.g., in [37, 71]. In this alternative method, synthetic turbulence is precomputed and stored on many discrete nested grids at different scales, with magnetic fluctuations between scales $l_{\min,i}$ and $l_{\max,i}$ with individual magnetic-field strengths $\delta B_i^2 = \delta B^2 (l_{\max,i}^{\xi-1} - l_{\min,i}^{\xi-1}) / (l_{\max}^{\xi-1} - l_{\min}^{\xi-1})$ and $l_{\max} \sim 5l_c$. We found agreement between results obtained using both methods.

Note that CRs below PeV energies diffuse on time scales smaller than the typical timescale of large-scale turbulence motions, justifying our approach of static turbulence. CRs are “frozen” within the ICM as the plasma evolves, as discussed in Section 2.

3.2 CR trajectories

Computing CR trajectories in magnetic fields involves solving the equation of motion for charged particles. These are then used to calculate the statistical transport characteristics of CRs. We use the Boris-push method for this task, as implemented in [5]. This captures the dynamics of charged particles in magnetic fields while preserving key properties, such as CR energy.

3.3 Model of small-angle scattering in magnetic micromirrors

We model the effect of magnetic micromirrors as a change of propagation after a distance s by an angle $\delta\theta$ given the scattering rate $\nu_{mm} = \delta\theta^2 c/s$. Particles traveling the mean free path $\lambda_{mm} = c/\nu_{mm}$ will have lost information of their original direction. At each step s , chosen to be smaller than λ_{mm} , we introduce a small deflection

$$\delta\theta = X \sqrt{\frac{s \nu_{mm}}{c}}, \quad (17)$$

where the random Gaussian variable X with mean 0 and standard deviation 1 represents the assumption that CRs random-walk their way through the magnetic micromirrors. Alternatively, micromirrors could be directly modeled in the magnetic field, which would, however, necessitate step sizes $s \lesssim l_{mm} \ll \lambda_{mm}$, leading to significantly longer simulation times.

3.4 Model of scattering at mesoscales

There is an ongoing debate about the dominant mechanism of CR scattering off mesoscale fluctuations, with theories including “extrinsic” (cascading) turbulence and “self-excitation” (by kinetic CR-driven instabilities) scenarios (see [52] and [43] for recent overviews). Here, we focus on the extrinsic scenario, with the self-excitation discussed in Section 2.

The CR diffusion coefficient due to resonant scattering is, by dimensional analysis,

$$\kappa_{\text{res}} \sim \frac{c r_g}{f(r_g)}, \quad (18)$$

where $f(r_g)$ is a dimensionless model-dependent numerical factor expressing the efficiency of the resonant scattering off turbulent magnetic structures at the scale $l \sim r_g$. Quasi-linear theory [49] determines this factor for isotropic turbulence as the fraction of the parallel turbulent power located at the gyroresonant scales $l = 2\pi/k_{\parallel} \sim r_g$, viz. $f(r_g) \sim \int_{2\pi/r_g}^{\infty} dk_{\parallel} P(k_{\parallel}) / (B^2/8\pi) \leq 1$, where k_{\parallel} is the parallel wavenumber and $P(k_{\parallel})$ is the parallel magnetic-energy spectrum. Assuming an undamped turbulent cascade with $P(k_{\parallel}) \propto k_{\parallel}^{-\xi}$ gives $f(r_g) \sim (r_g/l_c)^{\xi-1}$, where l_c is the energy-containing scale. Therefore,

$$\kappa_{\text{res}} \sim c l_c \left(\frac{r_g}{l_c} \right)^{2-\xi} \propto E^{2-\xi} l_c^{\xi-1} = E^{\delta} l_c^{-\delta+1}, \quad (19)$$

where $\delta = 2 - \xi$ is defined for convenience. In Section 1.2, we confirm this scaling via numerical simulations with unprecedented spatial resolution for a synthetic turbulence composed of plane waves.

An important qualitative result is that the cases $\delta = 2$ ($\xi = 0$)⁷ and $\delta = 1$ ($\xi = 1$)⁸ apply to $r_g \gg l_c$ and $r_g \sim l_c$, respectively, leaving only scalings with weaker energy dependence for $r_g \ll l_c$. In this limit, three popular choices for this scaling have appeared in the literature: (i) $\delta = 1/3$, corresponding to isotropic turbulence with a Kolmogorov [55] spectrum ($\xi = 5/3$); (ii) $\delta = 1/2$, corresponding to $\xi = 3/2$, which in the past was associated with the theory by Iroshnikov [46] and Kraichnan [59] for weak, isotropic magnetohydrodynamic (MHD) turbulence (now known not to exist); and (iii) $\delta = 0$, corresponding to the $\xi = 2$ Goldreich–Sridhar parallel spectrum of critically balanced Alfvénic turbulence ([38]; see [82] for a review) by adhering to (7) (note that this is not observed; see, e.g., [35]). Historically, Alfvénic turbulence was favored until it was realized that scale-dependent anisotropy [23, 28, 69], damping [43, 88], and intermittency [72, 86] might lead to inefficient gyroresonant scattering. A putative $\xi = 3/2$ cascade of fast MHD modes, if isotropic and robust against steepening [50, 52] and various damping mechanisms, may help by generating fluctuations with large enough frequencies and amplitudes to scatter CRs efficiently [27, 98]. More recently, the exponents $\delta = 1/3$ and $\delta = 1/2$ were ascribed to CR scattering in intermittent distributions of sharp magnetic-field bends in Goldreich–Sridhar turbulence [67] and in MHD turbulent dynamo [54]. Scaling exponents in the range $0.3 \lesssim \delta \lesssim 0.5$ are in broad agreement with constraints from Galactic observations (see [9] for a review).

3.5 Computation of CR diffusion coefficient

We use the CR propagation software CRPropa 3.2 [5] and extend the framework with our custom modules for the generalized nested turbulence,

⁷While there is no realistic turbulence model with $\xi = 0$, this case formally corresponds to the small-angle scattering limit of CRs with $r_g \gg l_c$: equation (7) then yields $\kappa \sim c r_g^2/l_c$, which is identical to (4) if one replaces l_{mm} and δB_{mm} with l_c and B , respectively. This is the standard theory for the high-energy regime referred to in the Introduction.

⁸The scaling (7) implies that Bohm diffusion ($\kappa_{\text{res}} \sim l_c r_g$) as the dominant process for $r_g \ll l_c$ is only possible for $\xi = 1$, which has not been observed to occur in realistic astrophysical environments over the whole turbulent cascade. Bohm diffusion, however, does apply at $r_g \sim l_c$ in the limit $\delta B \gg B_0$, where quasi-linear theory is expected to fail [75, 89, 93, 97].

different turbulence geometries, and micromirror scattering. We choose sufficiently small step sizes $s_{\text{step}} \sim \min\{\lambda_{\text{mm}}/10^3, \lambda_{\text{res}}/10^3, \lambda_{\text{he}}/10^3\}$, with mean free path $\lambda_i \sim \kappa_i/c$ to resolve the small-angle scattering at micromirrors, the resonant scattering in the extrinsic turbulent cascade, and the small-angle scattering in the high-energy limit, respectively. The option $\lambda_{\text{he}}/10^3$ is only included for CR energies above 10 EeV, as the high-energy limit is not valid below that energy. We compute sufficiently long CR trajectories $d \sim \min\{10^3 \lambda_{\text{mm}}, 10^3 \lambda_{\text{res}}, l_{\text{max}}\}$ (min is used here to save computation resources as only the more efficient scattering process needs to be resolved) for $E \lesssim 10$ EeV and $d \sim \max\{10^3 \lambda_{\text{he}}, l_{\text{max}}\}$ otherwise. The time-dependent diffusion coefficient $\kappa(t)$ for CRs performing a correlated random walk is [24]

$$\kappa(t) = \frac{\langle \Delta r^2 \rangle}{2t} \left(1 + \frac{2 \langle \cos \Theta \rangle}{1 - \langle \cos \Theta \rangle} \right) \stackrel{t \gtrsim \lambda/c}{\approx} \frac{\langle \Delta r^2 \rangle}{2t}, \quad (20)$$

with r representing the CR spatial displacement and the operation $\langle \dots \rangle$ averaging over CRs. The approximation for $t \gtrsim \lambda/c$ stems from the convergence to central-limit behavior, assuming that the deflection angles Θ are uniformly distributed after CRs travel a distance equivalent to their mean free path λ . We compute the steady-state diffusion coefficient κ by averaging over the value $\kappa(t)$ of 10^3 CRs. When using synthetic turbulence, we average the quantity over ten different realizations.

To compute the CR diffusion coefficients efficiently, we developed a recurrent neural network (RNN) that comprised a long short-term memory (LSTM) layer followed by a fully connected layer, linking the output of the LSTM to our output size, which is the predicted diffusion coefficient. This architecture allows us to capture the temporal dependencies in our data, making the network well-suited to use the CR trajectories as input for the model. For training data, we used trajectories generated by Monte Carlo simulations using the method described in Section 3.8, with various different effective diffusion coefficients. These effective diffusion coefficients served as labels for the training process. We chose low statistics of only 400 CRs for the 1D cases to illustrate the superiority of our neural network (trained on only 1600 CR trajectories in less than a minute on

a conventional CPU) over the classical computation of the running diffusion coefficient. We tested the convergence of the latter method to the theoretical expectation in the limit of large times and CR numbers and found good agreement. We demonstrate the capabilities of the model in Figure 4. The good performance of the network indicates that it could also be employed as a robust and transformative framework for assessing f_{mm} in MHD turbulence by propagating charged particles through the magnetic field. Reliable computation of the mean-squared diffusion coefficient requires many trajectories to deduce f_{mm} . Our use of a neural network demonstrates a concept for efficient trajectory classification and the computation of transport characteristics in astrophysical systems.

3.6 Micromirrors field from PIC simulations

The micromirror field shown in Fig. 1 was self-consistently generated using the hybrid-kinetic code PEGASUS++, which models the collisionless ions using a PIC method and the electrons as an isotropic, isothermal fluid. The code can simulate a plasma's expansion or contraction using a coordinate transform method (see [14] for further details), which via double-adiabatic conservation laws produces an ion pressure anisotropy that becomes mirror unstable.

In our simulation, we initialized a uniformly magnetized plasma ($\mathbf{B}_0 = B_0 \hat{\mathbf{x}}$) with a Maxwellian population (3000 ion macro-particles per cell) on a cubic domain. Its size is $L_0^3 = (76.8r_{g,i0})^3$, where $r_{g,i0}$ is the initial gyroradius of thermal ions, and the grid resolution is $\Delta x = 0.1r_{g,i0}$, $\Delta y = \Delta z = 0.3r_{g,i0}$. The initial ion plasma beta is $\beta_{i0} = 50$. The scale L_{\perp} of the plasma in the direction perpendicular to the background field then evolves as $L_{\perp} = L_0(1+t/\tau_{\text{crt}})^{-2}$, with a contraction timescale of $\tau_{\text{crt}} = 5 \times 10^3 \Omega_{i0}^{-1}$, while the parallel scale remains fixed. This gives rise to an ion pressure anisotropy $\Delta_i \equiv T_{\perp,i}/T_{\parallel,i} - 1 = (1+t/\tau_{\text{crt}})^2 - 1$ that increases with time. The mirror instability is triggered at $t \approx \tau_{\text{crt}}/2\beta_{i0} \simeq 0.01\tau_{\text{crt}}$, and then back-reacts at $t \approx 0.1\tau_{\text{crt}}$, entering the secular (i.e., power-law) phase of growth [63, 77]. The simulation is then run until $t_{\text{end}} \approx 0.25\tau_{\text{crt}}$. The snapshots of the field shown in Fig. 1 are taken at $t \approx 0.15\tau_{\text{crt}}$ and $t = t_{\text{end}}$, respectively.

Like all PIC simulations, the finite number of macroparticles in PEGASUS++ leads to grid-scale noise in the electromagnetic fields. To diagnose the influence of this noise on our calculation of CR propagation, we performed an experiment in which we removed the micromirrors from our PEGASUS++ simulation using a Fourier filter, and integrated CRs through the residual magnetic field. While the resulting diffusion coefficients show that PIC noise also leads to diffusive CR transport, their values are much larger than the ones associated with the micromirrors and so can be safely ignored (see Fig. 2).

3.7 Turbulence from MHD simulations

At macroscales, we computed CR diffusion coefficients in forced incompressible MHD turbulence from the John Hopkins Turbulence Databases⁹[34] to validate the consistency of our numerical approach that relies on synthetic turbulence. The MHD turbulence was generated in a direct numerical simulation of the incompressible MHD system of equations without guide fluid using 1024^3 nodes, employing a pseudo-spectral method, with energy input from a Taylor-Green flow stirring force.

3.8 Model of a static two-phase inhomogeneous medium

We model the CR transport through a two-phase inhomogeneous medium in 1D and in 3D (see a visualization in Figure 5). In 3D, we have modified the computationally intensive numerical experiment described in the previous subsections as follows: instead of imposing an additional effective scattering rate ν_{mm} on all CRs propagating through our turbulent field at all times and places, we now turn this scattering on only if the CR is seeing a magnetic field above a certain threshold $B_>$. This models qualitatively the fact that micromirrors are likely to appear in regions of more vigorous magnetic-field amplification. By varying $B_>$ between 0 and ∞ , we effectively vary the micromirror volume-filling fraction between 1 and 0, respectively. We assume the most intuitive

⁹Johns Hopkins Turbulence Databases, doi:10.7281/T1930RBS

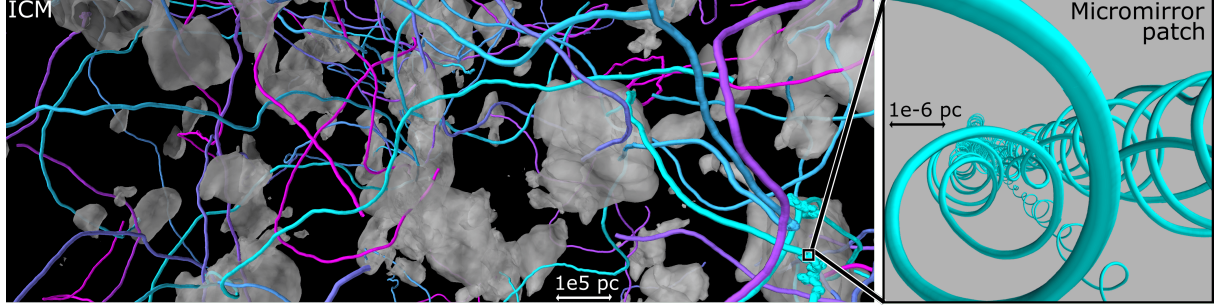


Fig. 5 Visualization of the numerical experiment described in Section 3.8 to study the effective CR transport in a two-phase medium. The grey surfaces are the isosurfaces of a threshold $B_>$. In our simplified numerical experiment, these isosurfaces enclose the micromirror patches, inside which the diffusion coefficient is much smaller than outside. Therefore, a given choice of $B_>$ corresponds to a certain value of f_{mm} (see Section 3.8). Example CR trajectories show increased deflections within the micromirror patches (see, e.g., lower right corner of the left panel and the zoom into a micromirror patch in the right panel). Taking the patches to be static is suitable for small f_{mm} as demonstrated in Section 3.8.

interpretation that this volume-filling fraction is the effective micromirror fraction f_{mm} in (10). As our estimate of the effective diffusion coefficient works in all dimensionalities, we also model the CR transport in a two-phase inhomogeneous medium in 1D. This allows us to compute diffusion coefficients effectively for many different values of f_{mm} . In doing so, we employ a simplified Monte Carlo model with $\nu(x) = \nu_{\text{mm}}$ for $x \bmod 1 \leq f_{\text{mm}}$ and $\nu(x) = \nu_{\text{res}}$ otherwise.

We now justify modeling micromirror patches experienced by diffusing CRs as static, based on the assumption of the short residence time of CRs in patches

$$\Delta t_p \sim \frac{l_p}{c}, \quad (21)$$

where l_p is the characteristic size of the patch. The residence time of CRs in a patch can be understood intuitively: when CRs penetrate a patch, they do so ballistically up to their mean free path $\lambda_{\text{mm}} \sim \kappa_{\text{mm}}/c$ for a time $\Delta t_{\text{bal}} \sim \lambda_{\text{mm}}/c$, followed by isotropic diffusion over a time Δt_{diff} . To get a rough estimate for Δt_{diff} , we can consider the simplified 1D case, where CRs exit either at the point of entry or at the point on the opposite end of the patch, with probabilities $p_1 \sim (l_p - \lambda_{\text{mm}})/l_p$ and $p_2 \sim \lambda_{\text{mm}}/l_p$, respectively. The corresponding times¹⁰ needed to exit the patch via diffusive transport are $\Delta t_1 \sim \lambda_{\text{mm}}^2/\kappa_{\text{mm}}$ and $\Delta t_2 \sim (l_p - \lambda_{\text{mm}})^2/\kappa_{\text{mm}}$. The mean time

duration of the diffusive transport is then given by

$$\begin{aligned} \Delta t_{\text{diff}} &\sim p_1 \Delta t_1 + p_2 \Delta t_2 \\ &\sim \frac{l_p - \lambda_{\text{mm}}}{l_p} \frac{\lambda_{\text{mm}}^2}{c \lambda_{\text{mm}}} + \frac{\lambda_{\text{mm}}}{l_p} \frac{(l_p - \lambda_{\text{mm}})^2}{c \lambda_{\text{mm}}} \\ &= \frac{l_p - \lambda_{\text{mm}}}{c}, \end{aligned} \quad (22)$$

resulting in $\Delta t_p \sim \Delta t_{\text{bal}} + \Delta t_{\text{diff}} \sim l_p/c$. Ref. [58] obtains this result by a more general method of solving the time-dependent diffusion equation. This result means that CRs with small diffusion coefficients, corresponding to short mean free paths, will exit the patch dominantly near their point of entry. In contrast, CRs with large diffusion coefficients traverse the patch (quasi)ballistically in time $\Delta t_p \sim \Delta t_{\text{bal}} \sim l_p/c$. As $\Delta t_{\text{diff}} \ll \Delta t_{\text{lifetime}}$, micromirrors can be treated as being static for most CRs.

Acknowledgments. PR thanks J. Becker Tjus, F. Effenberger, H. Fichtner, R. Grauer, J. Lübke, and L. Schlegel for valuable discussions on the usage of synthetic turbulence. AAS thanks E. Churazov and S. Komarov for useful discussions of the ICM and CR physics. The authors thank P. Oh, E. Quataert, L. Silva, L. Turica, D. Uzdensky, and especially W. Xu for insightful discussions of CR transport in the ICM. We also acknowledge the generous hospitality of the Wolfgang Pauli Institute, Vienna, where these ideas were discussed during the 14th Plasma Kinetics Working Meeting.

The work of PR was supported by a Gateway Fellowship. AFAB's work was supported by

¹⁰Note that in the limit $\lambda_{\text{mm}} \ll l_p$, $\Delta t_2 \sim l_p^2/c\lambda_{\text{mm}}$ can be larger than $\Delta t_{\text{lifetime}}$, meaning that patches cannot be treated as being static anymore. However, this only affects a small fraction $p_2 \sim \lambda_{\text{mm}}/l_p \ll 1$ of CRs.

a UKRI Future Leaders Fellowship (grant number MR/W006723/1). RJE's work was supported by a UK EPSRC studentship. MWK's work was supported in part by NSF CAREER Award No. 1944972. The work of AAS and GG was supported in part by a grant from STFC (ST/W000903/1). The work of AAS was also supported by a grant from EPSRC (EP/R034737/1) and by the Simons Foundation via a Simons Investigator Award. PK was supported by the Lyman Spitzer, Jr. Fellowship at Princeton University. UKRI is a Plan S funder, so for the purpose of Open Access, the author has applied a CC BY public copyright license to any Author Accepted Manuscript version arising from this submission.

Data availability. The simulation data presented in this paper are available upon reasonable request.

References

- [1] Ackermann M, et al (2014) *ApJ*787(1):18. <https://doi.org/10.1088/0004-637X/787/1/18>
- [2] Aerker S, Merten L, Becker Tjus J, et al (2023) arXiv e-prints p arXiv:2306.10802. <https://doi.org/10.48550/arXiv.2306.10802>
- [3] Ahlers M, Mertsch P (2017) *Progress in Particle and Nuclear Physics* 94:184–216. <https://doi.org/10.1016/j.ppnp.2017.01.004>
- [4] Aloisio R, Berezhinsky V (2004) *ApJ*612(2):900–913. <https://doi.org/10.1086/421869>
- [5] Alves Batista R, et al (2022) *J. Cosmology Astropart. Phys.*2022(9):035. <https://doi.org/10.1088/1475-7516/2022/09/035>
- [6] Amato E, Blasi P (2018) *Advances in Space Research* 62(10):2731–2749. <https://doi.org/10.1016/j.asr.2017.04.019>
- [7] Arzamasskiy L, Kunz MW, Squire J, et al (2023) *Physical Review X* 13(2):021014. <https://doi.org/10.1103/PhysRevX.13.021014>
- [8] Barnes A (1966) *Physics of Fluids* 9(8):1483–1495. <https://doi.org/10.1063/1.1761882>
- [9] Becker Tjus J, Merten L (2020) *Phys. Rep.*872:1–98. <https://doi.org/10.1016/j.physrep.2020.05.002>
- [10] Beduzzi L, Vazza F, Brunetti G, et al (2023) arXiv e-prints arXiv:2306.03764. <https://doi.org/10.48550/arXiv.2306.03764>
- [11] Blasi P, Amato E, Serpico PD (2012) *Phys. Rev. Lett.*109(6):061101. <https://doi.org/10.1103/PhysRevLett.109.061101>
- [12] Bonafede A, Feretti L, Murgia M, et al (2010) *A&A*513:A30. <https://doi.org/10.1051/0004-6361/200913696>
- [13] Böss LM, Steinwandel UP, Dolag K, et al (2023) *MNRAS*519(1):548–572. <https://doi.org/10.1093/mnras/stac3584>
- [14] Bott AFA, Arzamasskiy L, Kunz MW, et al (2021) *ApJ*922(2):L35. <https://doi.org/10.3847/2041-8213/ac37c2>
- [15] Bott AFA, Cowley SC, Schekochihin AA (2023) arXiv e-prints arXiv:2310.17754. <https://doi.org/10.48550/arXiv.2310.17754>
- [16] Brunetti G, Blasi P (2005) *MNRAS*363(4):1173–1187. <https://doi.org/10.1111/j.1365-2966.2005.09511.x>
- [17] Brunetti G, Lazarian A (2007) *MNRAS*378(1):245–275. <https://doi.org/10.1111/j.1365-2966.2007.11771.x>
- [18] Brunetti G, Lazarian A (2016) *MNRAS*458(3):2584–2595. <https://doi.org/10.1093/mnras/stw496>
- [19] Bustard C, Oh SP (2022) *ApJ*941(1):65. <https://doi.org/10.3847/1538-4357/aca021>
- [20] Butsky IS, Hopkins PF, Kempinski P, et al (2023) arXiv e-prints arXiv:2308.06316. <https://doi.org/10.48550/arXiv.2308.06316>
- [21] Cao Z, et al (2023) arXiv e-prints arXiv:2305.05372. <https://doi.org/10.48550/arXiv.2305.05372>
- [22] Cesarsky CJ, Kulsrud RM (1973) *ApJ*185:153–166. <https://doi.org/10.1086/152405>
- [23] Chandran BDG (2000) *Phys. Rev. Lett.*85(22):4656–4659. <https://doi.org/10.1103/PhysRevLett.85.4656>
- [24] Chen A, Renshaw E (1992) *Journal of Applied Probability* 29(4):792–813. <https://doi.org/10.2307/3214713>
- [25] Chen LE, et al (2020) *ApJ*892(2):114. <https://doi.org/10.3847/1538-4357/ab7a19>
- [26] Chew GF, Goldberger ML, Low FE (1956) *Proceedings of the Royal Society of London Series A* 236:112–118. <https://doi.org/10.1098/rspa.1956.0116>
- [27] Cho J, Lazarian A (2002) *Phys. Rev. Lett.*88(24):245001. <https://doi.org/10.1103/PhysRevLett.88.245001>
- [28] Cho J, Vishniac ET (2000) *ApJ*539(1):273–282. <https://doi.org/10.1086/309213>
- [29] Condorelli A, Biteau J, Adam R (2023) arXiv e-prints arXiv:2309.04380. <https://doi.org/10.48550/arXiv.2309.04380>
- [30] Consortium CTA, other (2023) arXiv e-prints arXiv:2309.03712. <https://doi.org/10.48550/arXiv.2309.03712>

[31] Cuciti V, et al (2022) *Nature*609(7929):911–914. <https://doi.org/10.1038/s41586-022-05149-3>

[32] De La Torre Luque P, Gaggero D, Grasso D, et al (2023) *A&A*672:A58. <https://doi.org/10.1051/0004-6361/202243714>

[33] Enßlin T, Pfrommer C, Miniati F, et al (2011) *A&A*527:A99. <https://doi.org/10.1051/0004-6361/201015652>

[34] Eyink G, Vishniac E, Lalescu C, et al (2013) *Nature*497(7450):466–469. <https://doi.org/10.1038/nature12128>

[35] Fornieri O, Gaggero D, Cerri SS, et al (2021) *MNRAS*502(4):5821–5838. <https://doi.org/10.1093/mnras/stab355>

[36] Giacalone J, Jokipii JR (1999) *ApJ*520(1):204–214. <https://doi.org/10.1086/307452>

[37] Giacinti G, Kachelrieß M, Semikoz DV, et al (2012) *J. Cosmology Astropart. Phys.*2012(7):031. <https://doi.org/10.1088/1475-7516/2012/07/031>

[38] Goldreich P, Sridhar S (1995) *ApJ*438:763. <https://doi.org/10.1086/175121>

[39] Govoni F, et al (2017) *A&A*603:A122. <https://doi.org/10.1051/0004-6361/201630349>

[40] Hall AN (1981) *MNRAS*197:977–993. <https://doi.org/10.1093/mnras/197.4.977>

[41] Hasegawa A (1969) *Physics of Fluids* 12:2642–2650. <https://doi.org/10.1063/1.1692407>

[42] Hopkins PF, Chan TK, Garrison-Kimmel S, et al (2020) *MNRAS*492(3):3465–3498. <https://doi.org/10.1093/mnras/stz3321>

[43] Hopkins PF, Squire J, Butsky IS, et al (2022) *MNRAS*517(4):5413–5448. <https://doi.org/10.1093/mnras/stac2909>

[44] Hussain S, Alves Batista R, de Gouveia Dal Pino EM, et al (2023) *Nature Communications* 14:2486. <https://doi.org/10.1038/s41467-023-38226-w>

[45] IceCube Collaboration (2022) *ApJ*938(2):L11. <https://doi.org/10.3847/2041-8213/ac966b>

[46] Iroshnikov PS (1964) *Soviet Ast.*7:566

[47] Jacob S, Pfrommer C (2017) *MNRAS*467(2):1449–1477. <https://doi.org/10.1093/mnras/stx131>

[48] Jacob S, Pfrommer C (2017) *MNRAS*467(2):1478–1495. <https://doi.org/10.1093/mnras/stx132>

[49] Jokipii JR (1966) *ApJ*146:480. <https://doi.org/10.1086/148912>

[50] Kadomtsev BB, Petviashvili VI (1973) *Soviet Physics Doklady* 18:115

[51] Kalnin JR, Kotomin E (1998) *Journal of Physics A Mathematical General* 31(35):7227–7234. <https://doi.org/10.1088/0305-4470/31/35/004>

[52] Kempinski P, Quataert E (2022) *MNRAS*514(1):657–674. <https://doi.org/10.1093/mnras/stac1240>

[53] Kempinski P, Quataert E, Squire J (2020) *MNRAS*493(4):5323–5335. <https://doi.org/10.1093/mnras/staa535>

[54] Kempinski P, Fielding DB, Quataert E, et al (2023) *MNRAS*525(4):4985–4998. <https://doi.org/10.1093/mnras/stad2609>

[55] Kolmogorov A (1941) *Akademii Nauk SSSR Doklady* 30:301–305

[56] Komarov SV, Churazov EM, Kunz MW, et al (2016) *MNRAS*460(1):467–477. <https://doi.org/10.1093/mnras/stw963>

[57] Kotera K, Lemoine M (2008) *Phys. Rev. D*77(2):023005. <https://doi.org/10.1103/PhysRevD.77.023005>

[58] Kotera K, Lemoine M (2008) *Phys. Rev. D*77(12):123003. <https://doi.org/10.1103/PhysRevD.77.123003>

[59] Kraichnan RH (1965) *Physics of Fluids* 8(7):1385–1387. <https://doi.org/10.1063/1.1761412>

[60] Krumholz MR, Crocker RM, Xu S, et al (2020) *MNRAS*493(2):2817–2833. <https://doi.org/10.1093/mnras/staa493>

[61] Kuhlen M, Phan VHM, Mertsch P (2022) *arXiv e-prints* arXiv:2211.05881. <https://doi.org/10.48550/arXiv.2211.05881>

[62] Kulsrud R, Pearce WP (1969) *ApJ*156:445. <https://doi.org/10.1086/149981>

[63] Kunz MW, Schekochihin AA, Stone JM (2014) *Phys. Rev. Lett.*112(20):205003. <https://doi.org/10.1103/PhysRevLett.112.205003>

[64] Kunz MW, Schekochihin AA, Chen CHK, et al (2015) *Journal of Plasma Physics* 81(5):325810501. <https://doi.org/10.1017/S0022377815000811>

[65] Kunz MW, Jones TW, Zhuravleva I (2022) In: *Handbook of X-ray and Gamma-ray Astrophysics*. Edited by Cosimo Bambi and Andrea Santangelo. Springer Nature Singapore, Singapore, https://doi.org/10.1007/978-981-16-4544-0_125-1

[66] Lazarian A, Xu S (2021) *ApJ*923(1):53. <https://doi.org/10.3847/1538-4357/ac2de9>

[67] Lemoine M (2023) *arXiv e-prints* arXiv:2304.03023. <https://doi.org/10.48550/arXiv.2304.03023>

[68] Ley F, Zweibel EG, Miller D, et al (2023) arXiv e-prints arXiv:2309.16751. <https://doi.org/10.48550/arXiv.2309.16751>

[69] Lithwick Y, Goldreich P (2001) *ApJ*562(1):279–296. <https://doi.org/10.1086/323470>

[70] Melville S, Schekochihin AA, Kunz MW (2016) *MNRAS*459(3):2701–2720. <https://doi.org/10.1093/mnras/stw793>

[71] Mertsch P (2020) *Ap&SS*365(8):135. <https://doi.org/10.1007/s10509-020-03832-3>

[72] Perri S, Pucci F, Malara F, et al (2019) *Sol. Phys.*294(3):34. <https://doi.org/10.1007/s11207-019-1421-y>

[73] Pfrommer C, Enßlin TA, Springel V (2008) *MNRAS*385(3):1211–1241. <https://doi.org/10.1111/j.1365-2966.2008.12956.x>

[74] Prokhorov DA, Churazov EM (2014) *A&A*567:A93. <https://doi.org/10.1051/0004-6361/201322454>

[75] Reichherzer P, Becker Tjus J, Zweibel EG, et al (2020) *MNRAS*498(4):5051–5064. <https://doi.org/10.1093/mnras/staa2533>

[76] Reichherzer P, Merten L, Dörner J, et al (2022) *SN Applied Sciences* 4:15. <https://doi.org/10.1007/s42452-021-04891-z>

[77] Rincon F, Schekochihin AA, Cowley SC (2015) *MNRAS*447:L45–L49. <https://doi.org/10.1093/mnrasl/slu179>

[78] Riquelme MA, Quataert E, Verscharen D (2015) *ApJ*800(1):27. <https://doi.org/10.1088/0004-637X/800/1/27>

[79] Rosin MS, Schekochihin AA, Rincon F, et al (2011) *MNRAS*413(1):7–38. <https://doi.org/10.1111/j.1365-2966.2010.17931.x>

[80] Ruszkowski M, Pfrommer C (2023) arXiv e-prints arXiv:2306.03141. <https://doi.org/10.48550/arXiv.2306.03141>

[81] Ruszkowski M, Enßlin TA, Brüggen M, et al (2008) *MNRAS*383(4):1359–1365. <https://doi.org/10.1111/j.1365-2966.2007.12659.x>

[82] Schekochihin AA (2022) *Journal of Plasma Physics* 88(5):155880501. <https://doi.org/10.1017/S0022377822000721>

[83] Schekochihin AA, Cowley SC, Kulsrud RM, et al (2005) *ApJ*629(1):139–142. <https://doi.org/10.1086/431202>

[84] Schlegel L, Frie A, Eichmann B, et al (2020) *ApJ*889(2):123. <https://doi.org/10.3847/1538-4357/ab643b>

[85] Shalaby M, Thomas T, Pfrommer C, et al (2023) arXiv e-prints arXiv:2305.18050. <https://doi.org/10.48550/arXiv.2305.18050>

[86] Shukurov A, Snodin AP, Seta A, et al (2017) *ApJ*839(1):L16. <https://doi.org/10.3847/2041-8213/aa6aa6>

[87] Skilling J (1971) *ApJ*170:265. <https://doi.org/10.1086/151210>

[88] Skilling J (1975) *MNRAS*173:255–269. <https://doi.org/10.1093/mnras/173.2.255>

[89] Snodin AP, Shukurov A, Sarson GR, et al (2016) *MNRAS*457(4):3975–3987. <https://doi.org/10.1093/mnras/stw217>

[90] Squire J, Kunz MW, Arzamasskiy L, et al (2023) *Journal of Plasma Physics* 89(4):905890417. <https://doi.org/10.1017/S0022377823000727>

[91] Steinwandel UP, Dolag K, Böss L, et al (2023) arXiv e-prints arXiv:2306.04692. <https://doi.org/10.48550/arXiv.2306.04692>

[92] Stuardi C, Bonafede A, Lovisari L, et al (2021) *MNRAS*502(2):2518–2535. <https://doi.org/10.1093/mnras/stab218>

[93] Subedi P, Sonsrettee W, Blasi P, et al (2017) *ApJ*837(2):140. <https://doi.org/10.3847/1538-4357/aa603a>

[94] Tautz RC, Dosch A (2013) *Physics of Plasmas* 20(2):022302. <https://doi.org/10.1063/1.4789861>

[95] Timokhin AN, Aharonian FA, Neronov AY (2004) *A&A*417:391–399. <https://doi.org/10.1051/0004-6361:20040004>

[96] van Weeren RJ, et al (2017) *Nature Astronomy* 1:0005. <https://doi.org/10.1038/s41550-016-0005>

[97] Vieu T, Reville B, Aharonian F (2022) *MNRAS*515(2):2256–2265. <https://doi.org/10.1093/mnras/stac1901>

[98] Yan H, Lazarian A (2002) *Phys. Rev. Lett.*89(28):281102. <https://doi.org/10.1103/PhysRevLett.89.281102>

[99] Yang Rz, Li GX, Wilhelm EdO, et al (2023) *Nature Astronomy* 7:351–358. <https://doi.org/10.1038/s41550-022-01868-9>

[100] Zhang R, Huang X, Xu ZH, et al (2023) arXiv e-prints arXiv:2305.06948. <https://doi.org/10.48550/arXiv.2305.06948>

[101] Zhou M, Zhdankin V, Kunz MW, et al (2023) arXiv e-prints arXiv:2308.01924. <https://doi.org/10.48550/arXiv.2308.01924>

[102] Zweibel EG (2013) *Physics of Plasmas* 20(5):055501. <https://doi.org/10.1063/1.4807033>

[103] Zweibel EG (2017) *Physics of Plasmas* 24(5):055402. <https://doi.org/10.1063/1.4984017>